Numerical Calculation of Conformally Smooth Hyperboloidal Data

Peter Hübner*

Max-Planck-Institut für Gravitationsphysik
Albert-Einstein-Institut
Am Mühlenberg 1
D-14476 Golm
FRG

This is the third paper in a series describing a numerical implementation of the conformal Einstein equation. This paper describes a scheme to calculate (three) dimensional data for the conformal field equations from a set of free functions. The actual implementation depends on the topology of the spacetime. We discuss the implementation and exemplary calculations for data leading to spacetimes with one spherical null infinity (asymptotically Minkowski) and for data leading to spacetimes with two toroidal null infinities (asymptotically A3). We also outline the (technical) modifications of the implementation needed to calculate data for spacetimes with two and more spherical null infinities (asymptotically Schwarzschild and asymptotically multiple black holes).

I. INTRODUCTION

In the conformal approach to numerical relativity we give data for the conformal field equations on a hyperboloidal initial slice and calculate the conformal spacetime (M, g_{ab}) determined by the data. The region on which the conformal factor Ω, which is one of our variables, is positive can be identified with a physical spacetime $(\tilde{M}, \tilde{g}_{ab})$ satisfying the Einstein equation. The boundary $\{\Omega = 0\}$ of this physical region represents future null infinity ($\mathcal{J}$) and possibly future timelike infinity (i^+).
Embedding the physical spacetime into a larger conformal spacetime implies a number of advantages over conventional approaches: Since null infinity is part of the grid, the determination of gravitational radiation is a well-defined and a gauge-ambiguity-free procedure. Furthermore we avoid any influence of artificial boundaries onto the result of our calculation, and we are enabled to use very efficient high order discretisation techniques, reducing the required computational resources by orders of magnitude.
In the first two papers [1, 2] in the series we have described the ideas behind the conformal approach, the general mathematical background, important properties of the time evolution equations, and the code used to integrate the time evolution equations.
To study properties of asymptotically flat solutions numerically, we need to provide initial data, i. e. we have to find solutions of the conformal constraints. In this paper we construct data for the conformal field equations by a formally infinite order scheme. The scheme consists of three basic elements, a Multigrid Newton Method to deal with the non-linearities,

*Electronic address: pth@aei-potsdam.mpg.de

pseudo-spectral techniques to achieve formally infinite order, and algebraic multigrid techniques to invert the linearised elliptic operators.
In section II we repeat the derivation of the Yamabe equation by the Lichnerowicz ansatz and discuss those properties of the solutions which are important for the numerical implementation by analytical and numerical means. In the next section we describe the strategy for calculating initial data, details of the numerical implementation for the cases leading to data for asymptotically Minkowski and asymptotically A3 spacetimes, and give the results of two exemplary calculations. In the last section we discuss how the scheme for the asymptotically Minkowski data can be extended to data for multiple black hole spacetimes by using well-established numerical techniques.
To avoid too many repetitions, we assume the reader to be familiar with the general approach as well as with the equations, both discussed in part I and II of this series [1, 2], and we shall refer to equation (n) of part N by writing (N/n). To the interested reader we should also point out the references [3, 4, 5, 6, 7] which describe a spherical symmetric (1D) and an axial symmetric (2D) implementation of the conformal field equations. There is also a recent review article by J. Frauendiener in *Living Reviews in Relativity* [8].

II. THE YAMABE EQUATION AND THE SMOOTHNESS OF ITS SOLUTIONS

A permissible set of data for the conformal time evolution equations is given by a set of functions which satisfy the conformal constraints. Finding initial data is hence equivalent to finding a solution to the conformal constraints.
The constraints of the conformal field equation (I/14) are regular on the whole conformal spacetime (M, g_{ab}), their principal part does not degenerate at $\mathcal{J}$. Therefore, it would be nice, if we could solve these constraints directly on our initial slice Σ_{t_0}. At present we do not know how to do that. The system of conformal constraints is a large coupled system of equations and, with the exception of the case of spherical symmetry [4], we do not know how to reduce it to a system to which known numerical techniques can be applied, e. g. a system of elliptic equations.
The way we construct initial data for the conformal field equations is an indirect one, we first solve the constraints of the vacuum Einstein equations and then construct the rest of the data from the conformal constraints. This amounts to providing a numerical implementation of the approach which has been used in [9] by L. Andersson, P. Chruściel, and H. Friedrich to prove existence of regular data for the conformal field equations. With this ansatz we are led to solving an elliptic equation of second order. A generalisation of the ansatz in [9] leads to a system of four coupled equations which has been analysed in [21]. We will restrict ourselves to the case of the ansatz of [9] for simplicity. In this case we already have the freedom to prescribe the conformal metric on the initial slice. Although this is not the full parameter space for the initial data, we expect to have covered enough of the parameter space to study interesting phenomenae.

A. The Yamabe equation

Let $\tilde{M}$ be an asymptotically flat spacetime and $\tilde{\Sigma}$ a hyperboloidal submanifold, i. e. a spacelike hypersurface extending to future null infinity. We denote by $\tilde{h}_{ab}$ the induced 3-metric, by $\tilde{k}_{ab}$ the induced second fundamental form, and by $\tilde{k}$ its trace. The Hamiltonian

constraint then reads

$$ {}^{(3)}\tilde{R} - \tilde{k}_{ab}\tilde{k}^{ab} + \tilde{k}^2 = 0, \tag{1} $$

where ${}^{(3)}\tilde{R}$ is the Ricci scalar associated with $\tilde{h}_{ab}$. If we denote by ${}^{(3)}\tilde{\nabla}_a$ the covariant derivative induced by $\tilde{h}_{ab}$, the vector constraint reads

$$ {}^{(3)}\tilde{\nabla}^b\tilde{k}_{ab} - {}^{(3)}\tilde{\nabla}_a\tilde{k} = 0. \tag{2} $$

We want to construct initial data representing this geometric situation. To simplify our calculation we assume that on our slice

$$ \tilde{k}_{ab} = \frac{1}{3}\tilde{h}_{ab}\tilde{k}. \tag{3a} $$

The vector constraint (2) implies

$$ \tilde{k} = \text{const} \neq 0. \tag{3b} $$

We assume

$$ \tilde{k} > 0. \tag{4} $$

Think of $\tilde{\Sigma}$ as being smoothly embedded into the conformal extension of our spacetime through future null infinity $\mathcal{J}^+$ and denote by $\bar{\Sigma}$ the closure of $\tilde{\Sigma}$ in this extension and by $\mathcal{S}$ the boundary of $\tilde{\Sigma}$. Let $\bar{\Omega}$ be a boundary defining function with non-vanishing gradient on $\mathcal{S}$, positive in the interior [22] and vanishing on $\mathcal{S}$, and let h_{ab} be an (almost) arbritrary metric on $\bar{\Sigma}$.

To reduce the Hamiltonian constraint (1) to an elliptic equation for a scalar function ϕ, we make the so-called Lichnerowicz ansatz, which reads in our case

$$ \tilde{h}_{ab} = \left(\frac{\bar{\Omega}}{\phi^2}\right)^{-2} h_{ab}. \tag{5} $$

With this ansatz $\tilde{h}_{ab}$ is singular at $\mathcal{S}$ indicating that $\mathcal{S}$ represents an infinity.

The Hamiltonian constraint becomes the so-called Yamabe equation,

$$ \begin{aligned} &4\,\bar{\Omega}^2\,{}^{(3)}\Delta\phi - 4\,\bar{\Omega}({}^{(3)}\nabla^a\bar{\Omega})({}^{(3)}\nabla_a\phi) \\ &\quad - \left(\frac{1}{2}\,{}^{(3)}R\,\bar{\Omega}^2 + 2\bar{\Omega}\,{}^{(3)}\Delta\bar{\Omega} - 3({}^{(3)}\nabla^a\bar{\Omega})({}^{(3)}\nabla_a\bar{\Omega})\right)\phi - \frac{1}{3}\tilde{k}^2\phi^5 = 0, \end{aligned} \tag{6} $$

where ${}^{(3)}\nabla_a$, ${}^{(3)}\Delta$, and ${}^{(3)}R$ are the covariant derivative, the Laplace operator, and the Ricci scalar associated with h_{ab}. The Yamabe equation is the equation, which we are going to solve numerically. It is an "elliptic" equation with a principal part which vanishes at the boundary.

After having solved the Yamabe equation (6) the remaining members of a minimal set of data which consists of $(h_{ab}, \Omega, k_{ab}, \Omega_0)$ (cf. II) are given by

$$ \Omega = \frac{\bar{\Omega}}{\phi^2} \tag{7} $$

$$ k_{ab} = \frac{1}{3}kh_{ab} \tag{8} $$

$$ \Omega_0 = \frac{1}{3}\left(\Omega k - \tilde{k}\right), \tag{9} $$

where k is an arbitrary function. Its choice is pure conformal gauge, it does not influence the physical spacetime obtained (cf. also [10, section 3] or [11, subsection 2.1.1]).
To calculate a complete set of data for the conformal field equations from a minimal set of data we use the conformal constraints to calculate $\gamma^a{}_{bc}$, ${}^{(0,1)}\hat{R}_a$, ${}^{(1,1)}\hat{R}_a{}^a$, Ω_a, ω, $f_{{}^{(1,1)}\hat{R}\,ab} := \Omega\,{}^{(1,1)}\hat{R}_{ab}$, $f_{B\,ab} := \Omega B_{ab}$, and $f_{E\,ab} = \Omega E_{ab} - 1/2\,{}^{(1,1)}\hat{R}_{ab}$ (cf. II for more details).
Due to our assumption (3a) the magnetic part of the Weyl tensor B_{ab} vanishes. For the case of vanishing conformal extrinsic curvature, i. e. $k = 0$, the quantity ${}^{(0,1)}\hat{R}_a$ also vanishes.
The following theorem by L. Andersson, P. Chruściel and H. Friedrich [9] gives existence and uniqueness of positive solutions to the Yamabe equation and guarantees regularity of ${}^{(1,1)}\hat{R}_{ab}$ and E_{ab}:

Theorem 1 (Andersson, Chruściel, Friedrich) *Suppose $(\bar{\Sigma}_{t_0}, h_{ab}, \bar{\Omega})$ is a 3-dimensional, orientable, compact, smooth Riemann space with boundary $\mathcal{S}$, $\bar{\Omega} = 0$ on $\mathcal{S}$ and positive elsewhere. Then there exists a unique positive solution ϕ of equation (6) and the following conditions are equivalent:*

1. *The function ϕ as well as the corresponding complete set of data, determined on the interior $\tilde{\Sigma}_{t_0}$ of $\bar{\Sigma}_{t_0}$, extend smoothly to all of $(\bar{\Sigma}_{t_0}, h_{ab})$.*
2. *The electric part of the conformal Weyl tensor ΩE_{ab} goes to zero at $\mathcal{S}$.*
3. *The extrinsic 2-curvature induced by h_{ab} on $\mathcal{S}$ is pure trace.*

If we did not require, that the extrinsic 2-curvature of $\mathcal{S}$ were pure trace, $f_{{}^{(1,1)}\hat{R}\,ab}$ and $f_{E\,ab}$ would not be vanishing on the boundary and therefore ${}^{(1,1)}\hat{R}_{ab}$ and E_{ab} would not be regular there. For this reason we choose the conformal 3-metric in such a way that the tracefree part of the extrinsic 2-curvature of $\mathcal{S}$ with respect to h_{ab} vanishes.
Observe that if we want to have a regular positive solution ϕ of (6) we cannot specify boundary values for ϕ on $\mathcal{S}$. Since for a regular solution the principle part vanishes at the boundary, we must have

$$(\nabla^a\bar{\Omega})(\nabla_a\bar{\Omega}) - \frac{\tilde{k}^2}{9}\phi^4\Big|_{\mathcal{S}} = 0. \tag{10}$$

B. Smoothness of solutions of the Yamabe equation on the initial slice

In our setup $\bar{\Sigma}_{t_0}$ will be a true subset of the initial slice Σ_{t_0} represented by the grid. To construct a complete set of data on Σ_{t_0} one is tempted to give $\bar{\Omega}$ and h_{ab} on Σ_{t_0} with $\bar{\Omega} \leq 0$ outside $\bar{\Sigma}_{t_0}$ and solve (6) on Σ_{t_0}. In the general case we obtain a complete set of data which is not continuous on $\mathcal{S}$. Since our discretisation of the time integrator requires sufficiently smooth data we cannot proceed this way. In the following we will give an argument, why we have to expect a non-continuity, and we will show a numerical example.

To calculate the curvature variables ${}^{(1,1)}\hat{R}_{ab}$ and E_{ab} from $f_{{}^{(1,1)}\hat{R}\,ab}$ and $f_{E\,ab}$ we have to divide by Ω. To calculate the limit for $\Omega \to 0$, which is the value at $\mathcal{S}$, we apply l'Hopital's rule and get

$$\frac{f}{\Omega}\bigg|_{\Omega=0} = \frac{{}^{(3)}\nabla^a\Omega\,{}^{(3)}\nabla_a f}{{}^{(3)}\nabla^a\Omega\,{}^{(3)}\nabla_a\Omega}. \tag{11}$$

For the highest derivatives of ϕ which appear in the expressions of ${}^{(1,1)}\hat{R}_{ab}$ and E_{ab} we find

$$ {}^{(1,1)}\hat{R}_{ab} \sim \partial^3\phi, \tag{12a} $$

$$ E_{ab} \sim \partial^4\phi\,. \tag{12b} $$

Let us now look at the following simple situation of figure 1. Suppose we have given a

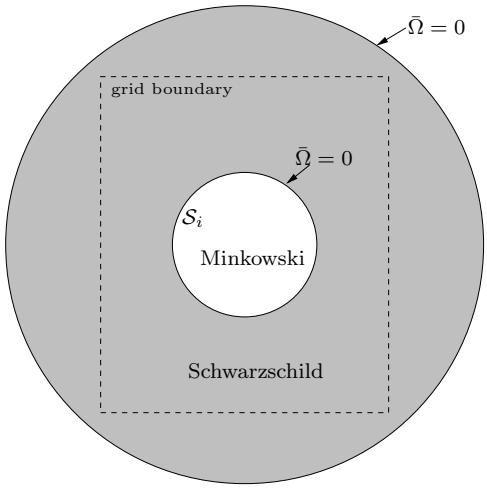

FIG. 1: A Kruskal-Schwarzschild slice enclosing a Minkowski slice.

spherical symmetric $\bar{\Omega}$, a spherical symmetric h_{ab} such that $\mathcal{S}_i$ is the unit sphere, and $k = 0$. Suppose $\bar{\Omega}$ is positive in the part labeled "Minkowski", which has one boundary diffeomorphic to S^2, and negative in the part labeled "Schwarzschild", which has two boundary components of topology S^2. Then, due to Birkhoff's theorem, $\{\bar{\Omega} > 0\}$ is a hyperboloidal slice of Minkowski spacetime, and $\{\bar{\Omega} < 0\}$ is a hyperboloidal slice of a Schwarzschild spacetime, since there are no spacelike slices in Minkowski space connecting two null infinities. The latter must have mass $m \neq 0$, whereas the mass of the Minkowski part necessarily vanishes. The Bondi mass of the initial slice is given by the integral over $\mathcal{S}$ with an integrand which is a polynomial expression of our variables involving components of E_{ab} [12]. Since the mass is 0, if we take the integral on the interior side, and non-vanishing, if we take the integral on the exterior side, the integrand cannot be continuous. The only source of the non-continuity can be the derivatives of ϕ. From the proof of theorem 1 it follows that ϕ is at least C^3 across the boundary $\mathcal{S}$. Since the highest derivatives of ϕ in E_{ab} are of fourth order, ϕ can in general not be C^4 across the boundary $\mathcal{S}$.

In a numerical code we would, of course, give boundary values for ϕ on the grid boundaries instead of specifying where the outer $\mathcal{S}$ is placed. However, unless we happen to prescribe by coincidence the appropriate boundary data on the grid boundary, we can expect to get the same behaviour. To check this hypothesis we have performed numerical test calculations for asymptotically A3 data with one Killing vector (a 2D calculation).

In the following we give the results of a typical numerical calculation. In this 2D calculation we have given the same free functions as in [7],

$$ \bar{\Omega} = \frac{1}{2}\left(1 - x^2\right) \tag{13a} $$

$$h_{xx} = 2e^{-2x\cos(y)} \tag{13b}$$
$$h_{xy} = 2\bar{\Omega}\left(x^2 - \sin(y^2)\right)e^{-x\cos(y)} \tag{13c}$$
$$h_{yy} = 2\left(1 + \bar{\Omega}^2\left(x^2 - \sin(y^2)\right)^2\right) \tag{13d}$$
$$h_{zz} = 2e^{-2x\cos(y)} \tag{13e}$$
$$k = 0, \tag{13f}$$

where $(x, y) \in [-1.4, 1.4] \times [-\pi, \pi]$. The free functions satisfy the regularity condition on $\mathcal{S}$. We then solve the Yamabe equation by discretising it by centered second order stencils, inverting the resulting sparse matrix with the AMG library [13, 14], and taking care of the non-linearities by a Multigrid Newton Method [15].
Although the free functions depend on both coordinates, we plot the results only for $y = -\pi/4$ for the reason of simpler graphics. The solution ϕ (solid line) for the calculation with the highest resolution performed, which is a 640×640 grid calculation, is shown in figure 2. We have also plotted the conformal factor Ω (dashed line) to indicate the location of the $\mathcal{S}$s

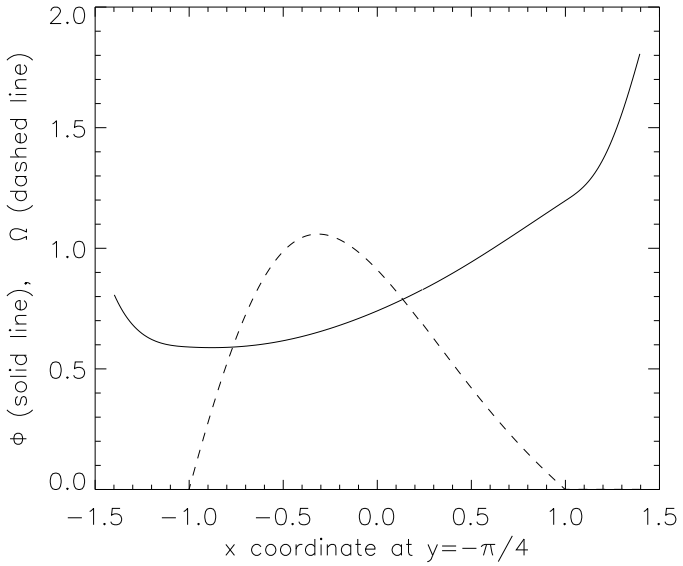

FIG. 2: Plot of ϕ (solid line) and Ω (dashed line) along the $y = \pi/4$ line.

at $x = -1$ and $x = 1$. The function ϕ seems to be perfectly smooth across the $\mathcal{S}$s.
By calculating the quantities ${}^{(1,1)}\hat{R}_{ab}$ and E_{ab} we see that this is not the case. To do so we use the second order scheme described in II. Figure 3 shows ${}^{(1,1)}\hat{R}_{\underline{xx}}$ for the grid sizes of 20×20, 40×40, 80×80, 160×160, 320×320, and 640×640 gridpoints (by ${}^{(1,1)}\hat{R}_{\underline{xx}}$ we denote the x coordinate components of the tensor ${}^{(1,1)}\hat{R}_{ab}$). Increasing line density correlates with finer grids. Obviously convergence near the two $\mathcal{S}$s is slow — the difference between the various grids is larger — and obviously ${}^{(1,1)}\hat{R}_{\underline{xx}}$ converges against a function which is only C^0 at the two $\mathcal{S}$s. This non-smoothness also explains the slow convergence rate.
Convergence is even slower in figure 4, where we plot $E_{\underline{xx}}$. The solution slowly converges to

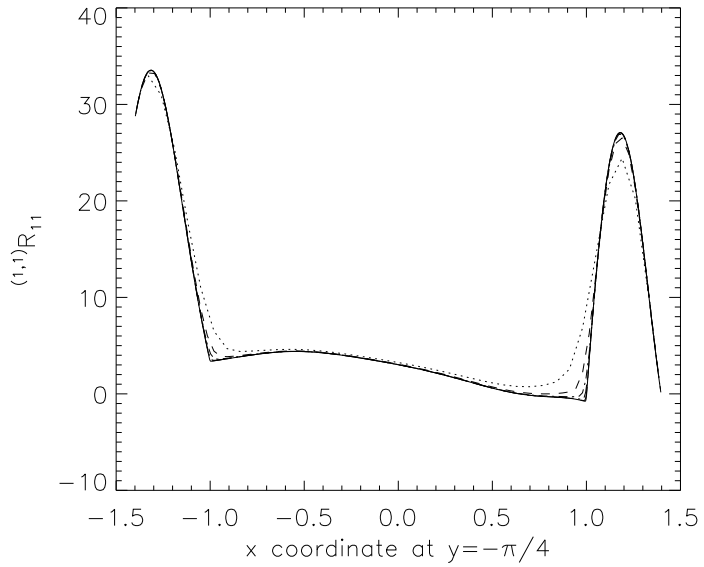

FIG. 3: ${}^{(1,1)}\hat{R}_{\underline{xx}}$ for grids from 20×20 (dotted line) to 640×640 (solid line).

a function with steps at the two $\mathcal{S}$s as expected from the theoretical considerations in the first part of the subsection.

III. CALCULATING EXTENDED HYPERBOLOIDAL INITIAL DATA — THE NUMERICAL IMPLEMENTATION

A. A rough description of the main ideas

What has been said in the previous section suggests the following strategy to calculate extended hyperboloidal initial data:

1. Solve the Yamabe equation (6) on $\bar{\Sigma}_{t_0}$ to get a minimal set of data.
2. Calculate a complete set of data on $\bar{\Sigma}_{t_0}$.
3. Smoothly extend the data from $\bar{\Sigma}_{t_0}$ to Σ_{t_0}.

The main part of the numerical implementation of step 1 and step 2 is solving "elliptic" equations with a principal part which degenerates at the boundary. To be able to obtain sufficient accuracy with an acceptable consumption of computer resources even without symmetry assumptions (3D) we use pseudo-spectral methods similar to the 2D calculations described in [7]. Since there exists a huge amount of literature on pseudo-spectral methods, we only very briefly describe our choices. The reader who wants to learn about the basics is referred to the literature, e. g. [16] for the general theory or [17] for other general relativistic applications.
Since pseudo-spectral methods are formally infinite order, the grid on which we discretise

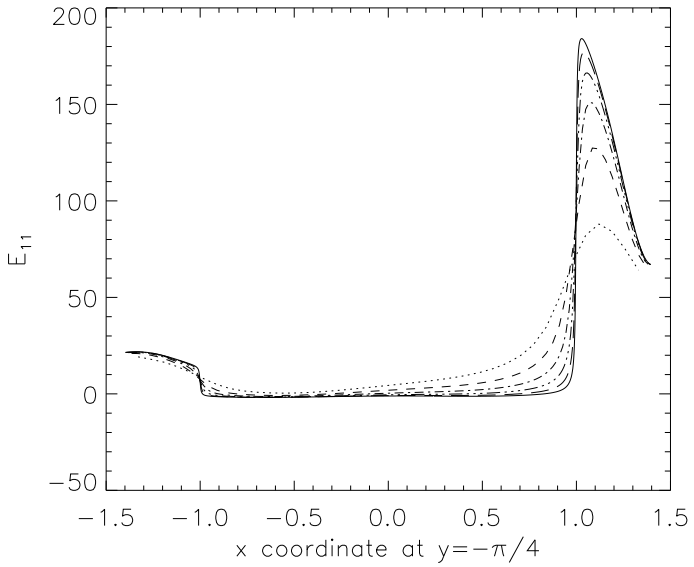

FIG. 4: $E_{\underline{xx}}$ for grids from 20×20 (dotted line) to 640×640 (solid line).

and invert the elliptic operator can be pretty coarse. The accuracy achieved is very high, as soon as the spectral grid resolution is sufficient to represent the structure of the solution. The limit of achievable accuracy is given by the accumulation of rounding errors in the fast Fourier transformation, the matrix inversion, and the consecutive solving of elliptic equations. Typically, using 32 gridpoints in each dimension is sufficient to achieve an accuracy which cannot be further improved.
For step 3 we use the representation of our variables in the spectral basis to calculate a smooth extension.

B. The Yamabe solver and the f/Ω divider

For simplicity we write the Yamabe equation in the form

$$\mathbf{E}\,\phi - \frac{1}{3}\tilde{k}^2\phi^5 = 0, \tag{14}$$

where $\mathbf{E}$ is a linear operator.
To deal with the nonlinearity we use the Multigrid Newton Method for nonlinear systems described in [15]:
Assuming we have given an approximate solution $\phi^{(n)}$ we calculate a hopefully better solution

$$\phi^{(n+1)} = \phi^{(n)} + \epsilon\,\delta\phi, \tag{15}$$

where the correction is the solution of

$$\mathbf{E}_l\delta\phi := \mathbf{E}\delta\phi - 5\left(\phi^{(n)}\right)^4\delta\phi = -\mathbf{E}\phi^{(n)} + \left(\phi^{(n)}\right)^5, \tag{16}$$

which is obtained by linearising the nonlinear equation (14). Since $\delta\phi$ is a correction to the solution, the order of the scheme and the eventual quality of the approximation depend on the order and the accuracy of the calculation of the residuum $-\mathbf{E}\phi^{(n)} + \left(\phi^{(n)}\right)^5$, but not on the discretisation of $\mathbf{E}_l$.
The value of the parameter ϵ is determined in the Multigrid Newton Method [15] by the following algorithm: We take the first value of ϵ in the sequence $1, \frac{1}{2}, \frac{1}{4}, \ldots$ for which

$$\|\mathbf{E}\phi^{(n+1)} - \left(\phi^{(n+1)}\right)^5\| \leq \left(1 - \frac{\epsilon}{2}\right) \|\mathbf{E}\phi^{(n)} - \left(\phi^{(n)}\right)^5\| \tag{17}$$

for an appropriate norm $\|.\|$, in our case the L_2 norm. This adaption of ϵ on each step stabilises the scheme and makes it less sensitive to a good initial guess $\phi^{(0)}$. Numerical experiments with a fixed ϵ were only stable for $\epsilon < 1/2^n$, where n is the dimension of the hypersurface $\bar{\Sigma}_{t_0}$.
The residuum is calculated by pseudo-spectral methods, which means, that from the values of $\phi^{(n)}$ at the gridpoints we calculate the spectral coefficients. Then we differentiate in the spectral space, where differentiation is essentially a multiplication, and transform back to the grid to get high order approximations of the derivatives. With these values of the derivatives we calculate the value of the residuum on the gridpoints.
The order of the differentiation with respect to a coordinate x^a is approximately the number of functions in the spectral basis for this coordinate, which is approximately the number of gridpoints in the corresponding dimension (a more accurate statement depends on the spectral basis, see below). Therefore the order of the differentiation increases with the number of gridpoints. This increase of the order with the number of gridpoints is called "formally infinite order".
For reasons of numerical efficiency the choice of the spectral basis is restricted to those bases for which we can use fast Fourier transformation (FFT) techniques to perform the transformation to and from the spectral space.
To perform the FFTs we use the FFTW library by M. Frigo and S. G. Johnson, which is a C subroutine library for computing the discrete Fourier transform (DFT) in one or more dimensions, of both real and complex data, and of arbitrary input size [18]. The library includes a parallel version for POSIX threads and the FFT is done by an $N \log N$ algorithm even if the prime factor decomposition of N contains large prime numbers. This has large advantages over simple $N \log N$ algorithms which are based on the assumption that the number of gridpoints N is a power of 2, e. g. when it comes to the issue of grid refinements in 3D.
The derivatives in the operator $\mathbf{E_l}$ are discretised by three point stencils. These stencils depend on the spacing of the grid which is given by the choice of the spectral basis. We are going to describe it below when we discuss the specific cases. Due to the dependence on the spectral basis we call this grid a spectral grid. In general the spectral grid does not coincide with the grid used for time evolution and is significantly coarser.
Where the boundary of the spectral grid coincides with $\mathcal{S}$, the initial approximation $\phi^{(0)}$ for the solution is chosen such that it coincides with (10) on $\mathcal{S}$. Then the boundary value for $\delta\phi$ is 0 in each iteration. If the grid boundary is inside physical spacetime, which is the case for more complicated forms of $\bar{\Sigma}_{t_0}$, where we need overlapping spectral grids to cover the physical part of the initial slice (multiple black holes, subsection IV), the boundary values for $\delta\phi$ are deduced from the other grids and iterated in a Schwarz alternating procedure.
After having provided boundary values we use algebraic multigrid techniques to solve for $\delta\phi$.

To do so we use the AMG library [13, 14], which was kindly provided to us by K. Stüben from the Gesellschaft für Mathematik und Datenverarbeitung. Different topologies of the spaces on which we solve the elliptic equations show up in different structures of the discretisation matrix of $\mathbf{E_l}$. Since AMG automatically derives a multigrid coarsening strategy from the structure of the discretisation matrix, only minor changes need to be made in the code which inverts the elliptic operator to adapt it to the various cases described below. This is a huge advantage. The price to pay is the fact, that the AMG library is the only part of the code which does not give excellent parallel scaling, in fact the AMG version used does not run in parallel at all. For a typical 3D run, which produces data for a time evolution grid of 100^3 or more gridpoints, the total time spent in the AMG library is of order of a few percent of the time spent in the rest of the code, although the rest has excellent parallel performance. Therefore, the non-scaling of the AMG part of the code is not a serious issue.

To calculate $g = f/\Omega$ we use the same numerical techniques applied to equation (II/7), which can formally be written as

$$\mathbf{G}g = F[f] \tag{18}$$

and has the "linearised" form

$$\mathbf{G}_l \delta g = -\mathbf{G}g^{(n)} + F[f]. \tag{19}$$

Observe that the metric used in (II/7) does not need to be identical with the 3-metric h_{ab}. And indeed, the code becomes much simpler if we use the diagonal Euclidean 3-metric δ_{ab}. As boundary values we use (II/8) on the grid boundaries which coincide with $\mathcal{S}$ and f/Ω on the grid boundaries which lie in the physical part. Of course, due to the latter, the grid boundaries which lie in the physical part must not intersect $\mathcal{S}$. As initial approximation we use a low order approximation of equation (II/7).
The attentive reader may ask the following. Equation (II/7) is a linear equation for g, what is the reason for doing an iteration which is typically used to deal with nonlinear terms.
The reason is very simple. If we discretised $\mathbf{G}$ to low order, we would get a sparse discretisation matrix, but also an inaccurate solution. If we discretised with high order stencils, we would get a not-very–sparse discretisation matrix, which is difficult to invert, and a complicated boundary treatment. By using the iteration on the linear equation we get a formally infinite order solution, which turns out to be very accurate, but we still have a sparse discretisation matrix. The repeated inversion of $\mathbf{G}_l$ is the price to pay.

C. The case of asymptotically A3 spacetimes

From the viewpoint of the initial data solver the simplest class of initial data are asymptotically A3 spacetimes. There the physical part $\tilde{\Sigma}_{t_0}$ of an initial slice has topology $R \times T^2$, and the boundary $\mathcal{S}$ consists of two two-dimensional tori T^2 (figure 4 of I). By doing an appropriate coordinate transformation within the initial data surface we can always ensure, that the coordinates y and z are 2π periodic and parametrise the two-dimensional torus [23], and that the two parts of the boundary $\mathcal{S}$, in the following called $\mathcal{S}_l$ and $\mathcal{S}_r$, are at constant x values $x = a$ and $x = b$. Although the code allows arbitrary values of a and b, as well as other periodicities in the y and z direction, we only describe the case with $a = -1$, $b = 1$, and 2π periodicity for simplicity.
Since y and z are 2π periodic we can simply use the Fourier functions $e^{i\,k_y\,y}$ and $e^{i\,k_z\,z}$ as basis

in the y and z direction. The spacing of the spectral grid in y and z direction is equidistant, the $N_{y,z}$ nodes of the spectral grid are placed at

$$y_j := \frac{2\pi j}{N_y} \tag{20a}$$

$$z_k := \frac{2\pi k}{N_z} \tag{20b}$$

In the x direction we use Chebychev polynomials

$$T_{k_x}(x) := \cos\left(k_x \arccos(x)\right). \tag{21}$$

The gridpoints are placed at the Gauss-Lobatto nodes

$$x_i := \cos\frac{\pi i}{N_x}, \tag{22}$$

where $N_x + 1$ is the number of gridpoints in the x direction.
For every function

$$f : [-1, 1] \to R, \tag{23}$$

there is a one-to-one relation to the function

$$f \circ cos : [0, \pi] \to R. \tag{24}$$

We can reduce the Chebychev transformation to a Fourier transformation, which of course can be treated by FFT techniques, by transferring the non-equidistant gridpoints in $[-1, 1]$ to equidistant gridpoints in $[0, \pi]$ and extending the range to the interval $[0, 2\pi[$ by applying the symmetry

$$\cos(\pi + x) = -\cos(x). \tag{25}$$

For a function $f(x, y, z)$ the spectral representation

$$f(x, y, z) := \sum_{k_x=0}^{N_x} \sum_{k_y=-N_y/2}^{N_y/2} \sum_{k_z=-N_z/2}^{N_z/2} a_{k_x k_y k_z} T_{k_x}(x) e^{i\,k_y\,y} e^{i\,k_z\,z} \tag{26}$$

is given by the coefficients $a_{k_x k_y k_z}$. Depending on N_y and N_z some of the coefficients are zero and due to the reality of f the complex numbers $a_{k_x k_y k_z}$ are not independent.
Then the coefficients ${a^{xyz}}_{k_x k_y k_z}$ of the derivatives ∂_{xyz} are given by

$${a^{y}}_{k_x k_y k_z} = k_y\, a_{k_x k_y k_z} \tag{27a}$$

$${a^{z}}_{k_x k_y k_z} = k_z\, a_{k_x k_y k_z} \tag{27b}$$

and the recursion relation

$$\begin{cases} {a^{x}}_{N_x k_y k_z} = {a^{x}}_{N_x+1\,k_y k_z} = 0 \\ c_{k_x} {a^{x}}_{k_x k_y k_z} = {a^{x}}_{k_x+2\,k_y k_z} + 2(k_x + 1){a^{x}}_{k_x+1\,k_y k_z}, \quad k_x = N_x - 1, \ldots, 0, \end{cases} \tag{27c}$$

where $c_0 = 2$ and $c_{k_x} = 1$ for $k_x \geq 1$.
Due to (27c) we loose one discretisation order with each ∂_x.

There exist FFT algorithms which take into account the even symmetries of the function (24), the so-called fast cosine transformations [19]. They are significantly more complicated than a normal FFT, but reduce the required space by a factor of 2 approximately. Since the space temporarily required in the initial data solver part of the code is significantly less than the space temporarily required in the time evolution part, we abstained from making use of the fast cosine transformation techniques and the implied memory savings.
Therefore, to calculate the spectral representation on the spectral grid, we proceed as follows: We first relabel the grid covering $[-1,1]\times[0,2\pi[\times[0,2\pi[$ to equidistantly cover $[0,\pi]\times[0,2\pi[\times[0,2\pi[$ and then extend it to $[0,2\pi[\times[0,2\pi[\times[0,2\pi[$. We use a three dimensional FFT for real numbers on the extended grid to calculate the spectral representation. Although our scheme can deal with any number of spectral gridpoints $(N_x,N_y,N_z)\geq(2,2,2)$, for reasons of numerical efficiency it is advisable to use values for which we get efficient FFTs. Of course, the large grid covering $[0,2\pi[\times[0,2\pi[\times[0,2\pi[$ is only used for calculating the spectral transformation and its inverse, tasks like calculating the residuum and the inversion of the discretisation matrix of $\mathbf{E}_l$ are performed on the original, smaller grid covering $[-1,1]\times[0,2\pi[\times[0,2\pi[$. The procedure for the inverse transformation is obvious from what has been said.
To derive the discretisation matrix of $\mathbf{E}_l$ we discretise the derivatives in $\mathbf{E}_l$ as follows

$$\partial_x f \to -\frac{x_{i+1}-x_i}{(x_{i+1}-x_{i-1})(x_i-x_{i-1})}f_{i-1,j,k}+\frac{(x_{i+1}-x_i)-(x_i-x_{i-1})}{(x_{i+1}-x_i)(x_i-x_{i-1})}f_{i,j,k} + \frac{x_i-x_{i-1}}{(x_{i+1}-x_{i-1})(x_{i+1}-x_i)}f_{i+1,j,k} \tag{28a}$$

$$\partial_y f \to -\frac{1}{y_{j+1}-y_{j-1}}f_{i,j-1,k}+\frac{1}{y_{j+1}-y_{j-1}}f_{i,j+1,k} \tag{28b}$$

$$\partial_z f \to -\frac{1}{z_{k+1}-z_{k-1}}f_{i,j,k-1}+\frac{1}{z_{k+1}-z_{k-1}}f_{i,j,k+1} \tag{28c}$$

$$\partial_x^2 f \to \frac{2}{(x_{i+1}-x_{i-1})(x_i-x_{i-1})}f_{i-1,j,k}-\frac{2}{(x_{i+1}-x_i)(x_i-x_{i-1})}f_{i,j,k} + \frac{2}{(x_{i+1}-x_{i-1})(x_{i+1}-x_i)}f_{i+1,j,k} \tag{28d}$$

$$\partial_y^2 f \to \frac{4}{(y_{j+1}-y_{j-1})^2}f_{i,j-1,k}-\frac{8}{(y_{j+1}-y_{j-1})^2}f_{i,j,k}+\frac{4}{(y_{j+1}-y_{j-1})^2}f_{i,j+1,k} \tag{28e}$$

$$\partial_z^2 f \to \frac{4}{(z_{k+1}-z_{k-1})^2}f_{i,j,k-1}-\frac{8}{(z_{k+1}-z_{k-1})^2}f_{i,j,k}+\frac{4}{(z_{k+1}-z_{k-1})^2}f_{i,j,k+1}\,. \tag{28f}$$

The mixed second derivatives are the obvious combinations of the first derivatives.
Combining the previous with subsection III B we have a very efficient elliptic solver for the Yamabe equation (cf. subsection III E for numbers). The solution of the Yamabe equation determines a minimal set of data.
Next we calculate the first and second derivatives of the minimal set of data by pseudo-spectral methods, which immediately leads to values for ${\gamma^a}_{bc}$, ${}^{(0,1)}\hat{R}_a$, ${}^{(1,1)}\hat{R}_a{}^a$, Ω_a, ω, $f_{{}^{(1,1)}\hat{R}\,ab}:=\Omega\,{}^{(1,1)}\hat{R}_{ab}$, and $f_{E\,ab}=\Omega E_{ab}-1/2\,{}^{(1,1)}\hat{R}_{ab}$ on the spectral grid. Due to assumption (3a) $f_{B\,ab}:=\Omega B_{ab}$ is identical 0.
To calculate ${}^{(1,1)}\hat{R}_{ab}$ and E_{ab} on the spectral grid we apply the procedure for dividing by Ω as outlined in the second part of subsection III B.
We now have a complete set of data on the spectral grid for $\bar{\Sigma}_{t_0}$. We need to transform these

data to the grid which is used in the time evolution and which extends beyond $\bar{\Sigma}_{t_0}$. Analytically we could just evaluate the sum in (26) for any (x, y, z) on the grid. Numerically that is not possible: For $|x| > 1$ the absolute value of the nth Chebychev polynomial grows as fast as $|x|^n$. Although the Chebychev coefficients of analytic functions decay exponentially fast for sufficiently large n, the numerically calculated coefficients do not decay to exactly 0 due to rounding errors, typically not larger than 10^{-11}, but non-vanishing. Due to the rapid growth of $|x|^n$ for large n, these rounding errors would dominate the numerical result. The described way of extending is therefore numerically unstable.
A possible solution goes as follows: For $|x| > 1$ we replace the Chebychev polynomials $T_k(x)$ by some functions $\tilde{T}_k(x)$ which fuse sufficiently smooth into the Chebychev polynomials at $|x| = 1$ and which have bounded growth. There are of course an unlimited number of options to do so, or choice is

$$\tilde{T}_k(x) = \begin{cases} (\mathrm{sign}x)^k \cosh\left(k \cosh^{-1}\tilde{x}\right) & |x| > 1 \\ \cos\left(k \cos^{-1}x\right) & |x| \leq 1 \end{cases} \tag{29}$$

with $\tilde{x} = \left(\tan\frac{k^2}{4}\left(x - \mathrm{sign}x\right)\right) \Big/ \left(\frac{k^2}{4}\right) + \mathrm{sign}x$. We call the process of calculating initial values on the time evolution grid from the spectral grid "extension procedure".

D. The case of spacetimes which are asymptotically Minkowski

Asymptotically Minkowski spacetimes are spacetimes whose null infinity has spherical cuts. Therefore the topology of $\bar{\Sigma}_{t_0}$ is the one of a three-dimensional ball (cf. figure 1 of I).
We assume that $(x^a) = (x, y, z)$ is a coordinate system induced by R^3, which we call a Cartesian coordinate system, and that the Cartesian components $h_{\underline{ab}}$ of the 3-metric h_{ab} are smooth. These are the coordinates in which the time evolution is done. We call the coordinate system (r, ϑ, φ) defined by

$$x = r \sin\vartheta \cos\varphi \tag{30a}$$
$$y = r \sin\vartheta \sin\varphi \tag{30b}$$
$$z = r \cos\vartheta \tag{30c}$$

the polar coordinate system $x^{a'}$. Without loss of generality we can assume that $\mathcal{S}$ coincides with the $r = 1$ coordinate surface. The interval $(r, \vartheta, \varphi) \in [0, 1] \times [0, \pi] \times [0, 2\pi[$ then covers the unit ball B^3.
Using polar coordinates has the advantage, that the boundary $\mathcal{S}$ coincides with a coordinate surface. On the other side we have to deal with the coordinate singularities at $\vartheta = 0$ or π (the z-axis) and $r = 0$ (the origin). The coordinate singularities cause singular behaviour of the metric and its derivatives and potentially lead to numerical instabilities. To avoid these, a careful choice of the placement of the grid nodes and special measures in the spectral transformation must be taken. In this paper we describe what we have done. The reader can find a more exhaustive discussion of what can be done in [20].
Apart from the changes enforced by the coordinate singularities, the code is very similar to the previous case of asymptotically A3 data.

Since any interval $[a, b]$ can easily be mapped to $[-1, 1]$, functions on any interval $[a, b]$ can be represented by Chebychev polynomials. Therefore, one could in principle work on the

r-interval $[0,1]$. Due to the coordinate singularities, this would not be a good idea. Firstly, there would be a Gauss-Lobatto node directly at the origin. And secondly, near the origin the gridpoints would be extremely dense. Instead of representing the ball by $[0,1]\times[0,\pi]\times[0,2\pi[$ we use $[-1,1]\times[0,\pi[\times[0,\pi[$ as minimal coordinate patch. By the symmetries

$$f(r,\vartheta+\pi,\varphi) = \pm f(-r,\vartheta,\varphi) \tag{31a}$$
$$f(r,\vartheta,\varphi+\pi) = \pm f(-r,\pi-\vartheta,\varphi), \tag{31b}$$

where the signs depend on what tensor component is represented by f, the use of the function (24) instead of (23), and the identity (25), this interval can be mapped to the interval $[0,2\pi[\times[0,2\pi[\times[0,2\pi[$, on which everything is 2π periodic. Spectral transformations are performed on this extended range $[0,2\pi[\times[0,2\pi[\times[0,2\pi[$. As in the previous section the use of the extended range is a waste of memory, but again this is not influencing the total memory requirements of the code.
Now we have to place the gridpoints in such a way that there is no gridpoint at the origin and on the axis. We use N_r+1 gridpoints, where N_r is odd, to cover the r-interval $[-1,1]$:

$$r_i = \cos(i\frac{\pi}{N_r}) \quad i = 0,\ldots,N_r\,. \tag{32a}$$

Since N_r is odd, there is no gridpoint at $r=0$. The interval $[0,2\pi[$ of the extended range is then covered by $2N_r$ gridpoints, i. e. 4 is not a divider of $2N_r$, and FFTs based on powers of 2 cannot be used.
To cover the ϑ-interval $[0,\pi[$ we use N_ϑ gridpoints which we place at

$$\vartheta_j = j\frac{\pi}{N_\vartheta} + \frac{\pi}{2N_\vartheta}, \quad j = 0,\ldots,N_\vartheta-1\,. \tag{32b}$$

The shift of $\frac{\pi}{2N_\vartheta}$ ensures, that there is no gridpoint at the axis. In total we have $2N_\vartheta$ gridpoints on the ϑ-interval $[0,2\pi[$.
To cover the φ-interval $[0,\pi[$ we use N_φ gridpoints which we place at

$$\varphi_k = k\frac{\pi}{N_\varphi}, \quad k = 0,\ldots,N_\varphi-1\,. \tag{32c}$$

There is no shift needed, any value of φ can be assumed. In total we have $2N_\varphi$ gridpoints on the φ-interval $[0,2\pi[$.
The discretisation of the derivative operators in $\mathbf{E_l}$ happens as in (28), where (x,y,z) is replaced by (r,ϑ,φ).
We now have a grid which avoids the coordinate singularities. This is still not sufficient to avoid numerical problems. The problems are caused by the components which behave like powers of $1/\sin(\vartheta)$ near the axis and/or like powers of $1/r$ near the origin. If we make a spectral transformation we always get significant values for the highest frequencies, no matter how many basis functions (=gridpoints) we use. These high frequencies make the Multigrid Newton Method unstable. To avoid the high frequencies we only apply spectral transformation to "regularised quantities". What we mean by "regularised quantities" will become obvious from what follows.

As free functions we give the Cartesian components $h_{\underline{ab}}$ of the 3-metric h_{ab}, $\bar{\Omega}$, and k as functions of the polar coordinates. We suppose that the Cartesian components of the metric

and k are given in a form which extends to the whole time evolution grid. The polar coordinate components $h_{\underline{a'}\underline{b'}}$ of the 3-metric h_{ab} are then given by

$$\begin{aligned}
h_{rr} &= (2c_\varphi c_\vartheta h_{xz} + 2c_\vartheta h_{yz} s_\varphi)\, s_\vartheta + h_{zz}(c_\vartheta)^2 + \left(2c_\varphi h_{xy} s_\varphi + h_{xx}(c_\varphi)^2 + h_{yy}(s_\varphi)^2\right)(s_\vartheta)^2 \\
&=: \bar{h}_{rr} && \text{(33a)} \\
h_{r\vartheta} &= r\Big[c_\varphi h_{xz}(c_\vartheta)^2 + h_{yz} s_\varphi (c_\vartheta)^2 + s_\vartheta\left(-(c_\vartheta h_{zz}) + 2c_\varphi c_\vartheta h_{xy} s_\varphi + c_\vartheta h_{xx}(c_\varphi)^2 + c_\vartheta h_{yy}(s_\varphi)^2\right) \\
&\qquad + (-c_\varphi h_{xz} - h_{yz} s_\varphi)(s_\vartheta)^2\Big] \\
&=: r\bar{h}_{r\vartheta} && \text{(33b)} \\
h_{r\varphi} &= r s_\vartheta\Big[(c_\varphi c_\vartheta h_{yz} - c_\vartheta h_{xz} s_\varphi) + \left(-c_\varphi h_{xx} s_\varphi + c_\varphi h_{yy} s_\varphi + h_{xy}(c_\varphi)^2 - h_{xy}(s_\varphi)^2\right) s_\vartheta\Big] \\
&=: r s_\vartheta \bar{h}_{r\varphi} && \text{(33c)} \\
h_{\vartheta\vartheta} &= r^2\Big[(-2c_\varphi c_\vartheta h_{xz} - 2c_\vartheta h_{yz} s_\varphi)\, s_\vartheta + 2c_\varphi h_{xy} s_\varphi (c_\vartheta)^2 + h_{xx}(c_\varphi)^2 (c_\vartheta)^2 \\
&\qquad + h_{yy}(c_\vartheta)^2 (s_\varphi)^2 + h_{zz}(s_\vartheta)^2\Big] \\
&=: r^2 \bar{h}_{\vartheta\vartheta} && \text{(33d)} \\
h_{\vartheta\varphi} &= r^2 s_\vartheta\Big[\left(-c_\varphi c_\vartheta h_{xx} s_\varphi + c_\varphi c_\vartheta h_{yy} s_\varphi + c_\vartheta h_{xy}(c_\varphi)^2 - c_\vartheta h_{xy}(s_\varphi)^2\right) + (-c_\varphi h_{yz} + h_{xz} s_\varphi)\, s_\vartheta\Big] \\
&=: r^2 s_\vartheta \bar{h}_{\vartheta\varphi} && \text{(33e)} \\
h_{\varphi\varphi} &= r^2 s_\vartheta^2\Big[-2c_\varphi h_{xy} s_\varphi + h_{yy}(c_\varphi)^2 + h_{xx}(s_\varphi)^2\Big] \\
&=: r^2 (s_\vartheta)^2 \bar{h}_{\varphi\varphi}, && \text{(33f)}
\end{aligned}$$

where $c_\vartheta := \cos\vartheta$, $c_\varphi := \cos\varphi$, $s_\vartheta := \sin\vartheta$, $s_\varphi := \sin\varphi$, and we have written h_{rr} although we really mean $h_{\underline{r}\underline{r}}$. The inverse metric h^{ab} can then be written as

$$h^{\underline{a'}\underline{b'}} = \begin{pmatrix} \bar{h}^{rr} & \frac{1}{r}\bar{h}^{r\vartheta} & \frac{1}{r\sin\vartheta}\bar{h}^{r\varphi} \\ \frac{1}{r}\bar{h}^{r\vartheta} & \frac{1}{r^2}\bar{h}^{\vartheta\vartheta} & \frac{1}{r^2\sin\vartheta}\bar{h}^{\vartheta\varphi} \\ \frac{1}{r\sin\vartheta}\bar{h}^{r\varphi} & \frac{1}{r^2\sin\vartheta}\bar{h}^{\vartheta\varphi} & \frac{1}{(r\sin\vartheta)^2}\bar{h}^{\varphi\varphi} \end{pmatrix}, \qquad (34)$$

where $\bar{h}^{\underline{a'}\underline{b'}}$ is the inverse of the matrix $\bar{h}_{\underline{a'}\underline{b'}}$.

To calculate the polar coordinate components $\gamma^{\underline{a'}}{}_{\underline{b'}\underline{c'}}$ of the 3-Christoffel symbols $\gamma^a{}_{bc}$ and the 3-Ricci scalar ${}^{(3)}R$, which contains derivatives of the $\gamma^{\underline{a'}}{}_{\underline{b'}\underline{c'}}$s, we first calculate the first and second derivatives of the "regularised quantities" $\bar{h}_{\underline{a'}\underline{b'}}$ and $\bar{h}^{\underline{a'}\underline{b'}}$ by spectral techniques, and then put in the singular terms by hand. This avoids the high frequency problem mentioned above.

The solution ϕ of the Yamabe equation (6) is then calculated as a function of the polar coordinates as before. Since the scalar ϕ is regular on the axis and at the center, no regularisation is needed.

From the solution ϕ we calculate a complete set of conformal data as follows. The Cartesian components of h_{ab} are taken from the free functions evaluated at the gridpoints. Then, the Cartesian components of the $\gamma^a{}_{bc}$s are obtained by fourth order differentiation ($II/10a$) on the time evolution grid. We do not use the extension procedure for the $\gamma^a{}_{bc}$s for two reasons. Firstly, the extension procedure is slow. And secondly, transforming the polar coordinate components of the $\gamma^a{}_{bc}$s to Cartesian components requires a careful treatment of the regularity conditions. As price for this convenience we get only 4th order approximations of the

Cartesian components of ${\gamma^a}_{bc}$ on the time evolution grid instead of infinite order approximations. But even if we started with infinite order data, after some time steps everything would only be 4th order, since the time evolution scheme is "only" 4th order.
Then we use the extrapolation procedure to calculate Ω on the whole grid. The spatial derivatives Ω_a of Ω are again obtained by fourth order differentiation. The time derivative Ω_0 of Ω is calculated from the free function on the time evolution grid directly.
The scalar ω is calculated on the spectral grid and then extended. The quantities ${}^{(0,1)}\hat{R}_a$, $f_{{}^{(1,1)}\hat{R}_{ab}}$, and $f_{E_{ab}}$ are tensor components. We first calculate the polar components on the spectral grid and then transform to Cartesian components. To the Cartesian components of ${}^{(0,1)}\hat{R}_a$ we apply the extension procedure.
The Ω division is applied to the Cartesian components of $f_{{}^{(1,1)}\hat{R}_{ab}}$ and $f_{E_{ab}}$ on the spectral grid. This leads to the Cartesian components of ${}^{(1,1)}\hat{R}_{ab}$ and E_{ab}. We complete the construction of the complete set of initial data by extending those to the time evolution grid.

E. Two examples

In this subsection we give two examples for initial data calculated with the solvers described above. The first example is an asymptotically A3 data set, the second an asymptotically Minkowski data set. We have given very general free functions. The purpose is to demonstrate the performance of the code described. In a realistic parameter study one would probably choose much simpler free functions.

For the asymptotically A3 case we have chosen

$$\bar{\Omega} = \frac{1}{2}\left(1 - x^2\right) \tag{35a}$$

$$h_{\underline{ab}} = \begin{pmatrix} 1 + \bar{\Omega}^2(\sin y)^2 & \frac{1}{4}\bar{\Omega}^2\left(x^2 - (\sin y)^2\right) & \frac{1}{4}\bar{\Omega}^2(\cos z)^2 \\ \frac{1}{4}\bar{\Omega}^2\left(x^2 - (\sin y)^2\right) & 1 + \bar{\Omega}^2(\sin z)^2 & \frac{1}{5}\bar{\Omega}^2\cos(x\pi) \\ \frac{1}{4}\bar{\Omega}^2(\cos z)^2 & \frac{1}{5}\bar{\Omega}^2\cos(x\pi) & 1 + \frac{1}{2}\bar{\Omega}^2 \end{pmatrix} \tag{35b}$$

$$k = \cos y. \tag{35c}$$

Without the $\bar{\Omega}^2$ terms, the choice of $h_{\underline{ab}}$ leads to data for an A3 spacetime.
Figure 5 shows the convergence of the violation of the constraint ${}^{(3)}\nabla_b {E_{\underline{x}}}^b + {}^{(3)}\epsilon_{\underline{x}bc}k^{bd}{B_d}^c = 0$ (II/14d, with $a = \underline{x}$), which is the constraint which shows the largest violation, for increasing spectral grid density. For simplicity we have plotted the L_2 norm over (y, z) as defined in (II/30). We observe that the violation is rapidly going to 0 as could be expected.
As we have 90 constraints and the violation of (II/14d,$a = \underline{x}$) dominates for all spectral resolutions, the average violation of constraints is more than by a factor of 50 less.
For these runs we stopped the Multigrid Newton Method iteration when the L_2 residuum dropped below 10^{-7}, at that time the approximation changed only by an order of 10^{-11} per iteration. To achieve such a small residuum we typically need less than 20 Iterations, which means that the average improvement of the residuum per iteration is a factor of 3.
For the $33 \times 32 \times 32$ spectral grid the average computer time per AMG step, the non-parallel part of the code, is about 10s for the Yamabe equation and 5s for the f/Ω steps on our SGI Origin 2000 with MIPS R10000 processors.

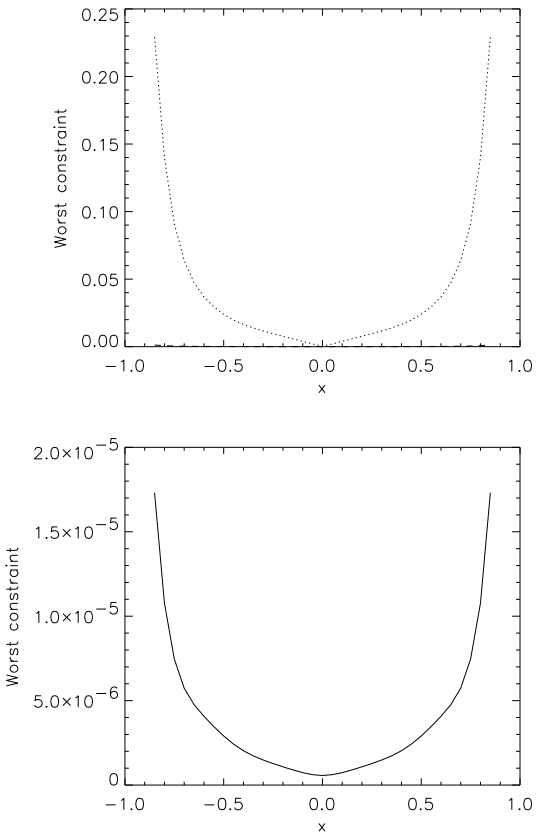

FIG. 5: Plots of the numerical violation of the constraint (II/14d,$a = \underline{x}$), which is the constraint with the largest violation, on a 50^3 time evolution grid for the data calculated from a $17 \times 16 \times 16$ (dotted line), a $25 \times 24 \times 24$ (dashed line, almost invisible, since very close to the abscissa), and a $33 \times 32 \times 32$ (solid line) spectral grid.

For the asymptotically Minkowski case we have chosen

$$\bar{\Omega} = \frac{1}{2}\left(1 - \left(x^2 + y^2 + z^2\right)\right) \tag{36a}$$

$$h_{\underline{ab}} = \begin{pmatrix} 1 + \bar{\Omega}^2 \cos y & \frac{1}{4}\bar{\Omega}^2\left((\cos x)^2 - (\sin y)^2\right) & \frac{1}{4}\bar{\Omega}^2(\cos z)^2 \\ \frac{1}{4}\bar{\Omega}^2\left((\cos x)^2 - (\sin y)^2\right) & 1 + \bar{\Omega}^2(\sin z)^2 & \frac{1}{5}\bar{\Omega}^2 \cos x \\ \frac{1}{4}\bar{\Omega}^2(\cos z)^2 & \frac{1}{5}\bar{\Omega}^2 \cos x & 1 + \frac{1}{2}\bar{\Omega}^2 \end{pmatrix} \tag{36b}$$

$$k = \cos z. \tag{36c}$$

Without the $\bar{\Omega}^2$ terms, the choice of $h_{\underline{ab}}$ leads to data for Minkowski space.
Figure 6 shows the average violation (II/30) of the constraints. In this example the violation of the constraints is not dominated by a single constraint as in the asymptotically A3 example. The class of constraints with the largest violations are (II/14j), then followed by (II/14d) and (II/14g).
As in the asymptotically A3 example the violation of the constraints is rapidly decreasing with the number of gridpoints in the spectral grid. For figure 6 we used a $34 \times 32 \times 32$ spectral grid. The violation of the constraints drops by a factor of ≈ 8, when we refine the

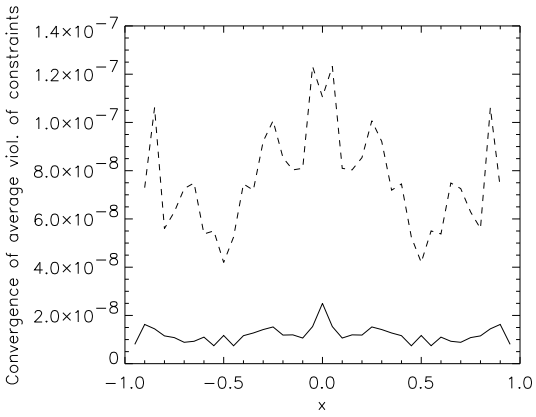

FIG. 6: Average violation of the constraints on a 50^3 (dashed line) and a 100^3 (solid line) time evolution grid for data calculated from a $34 \times 32 \times 32$ spectral grid.

time evolution grid, on which we numerically evaluate the constraints, from 50^3 to 100^3. If the data were an exact solution of the constraints, this factor would be ≈ 16. If the data were a bad solution of the constraints, this factor would be ≈ 1. Therefore we conclude that the data must be very close to an exact solution of the constraints.

IV. THE CASE OF MULTIPLE BLACK HOLE SPACETIMES

In the previous two subsections we have described in detail how initial data for the conformal field equations can be constructed for the asymptotically Minkowski and the asymptotically A3 case. The cases described are spacetimes with gravitational wave content. Depending on the "size" of the data, the gravitational waves may disperse to null infinity or may interact to form black holes. For our understanding of the Einstein equation it is certainly very interesting to study those cases, but as models for sources of gravitational waves they are probably not the most interesting ones. Therefore, the method for calculating initial data as described would only be of limited use, if it could not be extended to the case of one or more black holes (see figures 2 and 3 of I). In the following we describe how one can build a code to calculate data describing multiple black holes.

The case of one black hole with radiation (asymptotically Schwarzschild) is a straightforward extension of the asymptotically Minkowski case, since we can also use polar coordinates. Without loss of generality we can choose $\bar{\Omega}$ such that the inner $\mathcal{S}_i$ coincides with the coordinate sphere at $r_i > 0$ and the outer $\mathcal{S}_o$ coincides with the coordinate sphere at $r_o > r_i$. Instead of using $[-1,1] \times [0,\pi[\times [0,\pi[$ to cover the physical part of the grid, we use $[r_i, r_o] \times [0,\pi[\times [0,2\pi[$. Regularisation is even easier, since $r = 0$ is not part of $\bar{\Sigma}_{t_0}$, there is only an axis singularity but not an origin singularity to deal with.
When extending to the time evolution grid inside $\mathcal{S}_i$ more care is needed than in the asymp-

totically Minkowski case, since we extend onto the $r = 0$ coordinate singularity of the time evolution grid. When extending towards $r = 0$ the limit must not depend on the direction.

The case of two black holes is significantly more complex. Since we do not see how to cover $\bar{\Sigma}_{t_0}$ with a coordinate system for which we can also provide a spectral basis and fast spectral transformation algorithms, we suggest to use domain decomposition techniques.
In figure 7 we give our three coordinate patches. One boundary of each patch coincides with

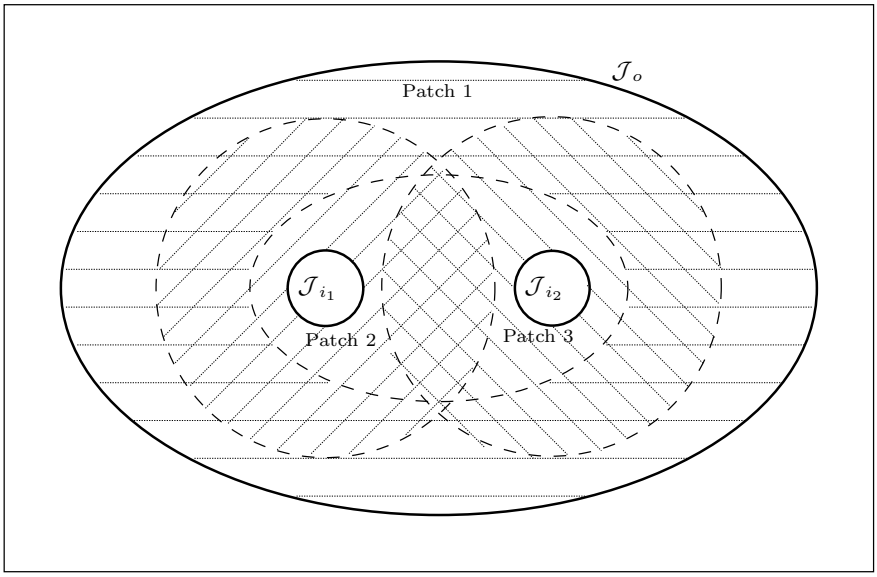

FIG. 7: Patches for pseudo-spectral grids to cover the initial slice of a two black hole spacetime. Dashed lines mark the interior boundaries on which boundary values are read off from the other patches.

a part of $\mathcal{S}$, the other, the dashed lines, in future called $\mathcal{G}$, lies inside $\bar{\Sigma}_{t_0}$ and inside at least one of the other patches. If we knew boundary values on $\mathcal{G}$, we would have three copies of the asymptotically Schwarzschild case — the elliptical shape of patch 1 is easily dealt with by a straightforward coordinate transformation. In the case of the f/Ω divider we do know the boundary values at $\mathcal{G}$, namely f/Ω, for the Yamabe equation we do not the boundary values at $\mathcal{G}$.
To provide boundary values on $\mathcal{G}$ we can use the Schwarz alternating procedure as described in section 6.4.1 of [16]: When solving the equation in one patch we read off the boundary values on $\mathcal{G}$ from the grids covering the other patches. By iteratively solving the equation on all patches we calculate a solution on $\bar{\Sigma}_{t_0}$. The book [16] contains a proof, that the Schwarz alternating procedure converges for the Laplace equation. The convergence rate depends on the overlap of the patches, the larger the overlap the better. In the overlap regions of our patches equation (6) is a normal elliptic equation, the principal part does not degenerate there. Therefore, it should in principle be possible to also prove convergence of the Schwarz alternating procedure for equation (6).

V. CONCLUSION

In this paper we have described a highly efficient and accurate scheme to calculate data for the conformal field equations without making any symmetry assumptions. The data are specified by giving a boundary defining function $\bar{\Omega}$ and the six components of the conformal 3-metric h_{ab}.

Acknowledgement

I would like to thank H. Friedrich for his help and support and J. Frauendiener for many helpful discussions on pseudo-spectral methods.
B. Schmidt, M. Weaver, and S. Husa should also be mentioned for many discussions.
I also acknowledge K. Stüben from the Gesellschaft für Mathematik und Datenverarbeitung, who put the Algebraic Multigrid Library AMG at my disposal, and M. Frigo and S. G. Johnson who wrote FFTW and made it publically available for the scientific community.

---

[1] P. Hübner, Class. Quantum Grav. **16**, 2145 (1999).
[2] P. Hübner, Class. Quantum Grav. **16**, 2823 (1999).
[3] P. Hübner, *Numerische und analytische Untersuchungen von (singulären,) asymptotisch flachen Raumzeiten mit konformen Techniken*, Ph.D. thesis, Ludwig-Maximilians-Universität München (1993).
[4] P. Hübner, Phys. Rev. D **53**(2), 701 (1996).
[5] J. Frauendiener, Phys. Rev. D **58**(6), 064002/1 (1998).
[6] J. Frauendiener, Phys. Rev. D **58**(6), 064003/1 (1998).
[7] J. Frauendiener, J. Comp. Appl. Math. **109**, 475 (1999).
[8] J. Frauendiener, Liv. Rev. in Relativity (2000).
[9] L. Andersson, P. T. Chruscíel, and H. Friedrich, Comm. Math. Phys. **149**, 587 (1992).
[10] H. Friedrich, Commun. Math. Phys. **91**, 445 (1983).
[11] P. Hübner, Class. Quant. Grav. **12**, 791 (1995).
[12] P. Hübner and M. Weaver, in preparation.
[13] K. Stüben, GMD report (1999).
[14] J. W. Ruge and K. Stüben, in *Multigrid Methods*, edited by S. F. McCormick, SIAM (Society for Industrial and Applied Mathematics, Philadelphia, 1987), pp. 73–130.
[15] D. Braess, *Finite Elemente* (Springer, Berlin, 1997).
[16] A. Quarteroni and A. Valli, *Numerical Approximation of Partial Differential Equations*, vol. 23 of *Springer Series in Computational Mathematics* (Springer, Berlin, 1997), 2nd ed.
[17] S. Bonazzola, J. Frieben, E. Gourgoulhon, and J. A. Marck, gr-qc **9604029**, 1 (1996).
[18] M. Frigo and S. G. Johnson, in *1998 ICASSP conference proceedings, Vol. 3* (ICASSP, 1998), p. 1381.
[19] C. Van Loan, *Computational Frameworks for the Fast Fourier Transform*, vol. 10 of *Frontiers in Applied Mathematics* (SIAM, Philadelphia, 1992).
[20] S. Bonazzola and J.-A. Marck, J. Comp. Phys. **87**, 201 (1990).
[21] L. Andersson and P. T. Chruściel, Dissertationes Mathematice pp. 1–100 (1996).

[22] The choice of the sign is arbitrary, since the conformal and the physical metric are connected by the square of the conformal factor.

[23] We describe the 3D code here. We also have a 2D code, where we made use of the simplifications implied by an hypersurface orthogonal Killing vector $\partial_z{}^a$. From the description of the 3D code, the 2D code should be obvious.